Electrogenic Proton-Pumping Capabilities of the M-Fast and M-Slow Photocycles of Bacteriorhodopsin[†,‡]

Richard W. Hendler*[,§,||] and Curtis W. Meuse[||]

Laboratory of Cell Biology, National Heart, Lung, and Blood Institute, National Institutes of Health, Bethesda, Maryland 20892, and Biospectroscopy Group, Biochemical Science Division, National Institute of Standards and Technology, Gaithersburg, Maryland 20899

Received August 28, 2007; Revised Manuscript Received January 16, 2008

ABSTRACT: The parallel model for the bacteriorhodopsin (BR) photocycle at neutral pH and a temperature near 20 °C contains an M-fast cycle with steps BR → K → L → M_f → N → O → BR and an M-slow cycle which contains steps BR → K → L → M_s → BR. With increasing actinic laser strength, the M-fast cycle at first rises faster than the M-slow cycle, but reaches saturation sooner and at a lower level than the M-slow cycle. The O-intermediate shows the same saturation behavior as M_f. In this paper, we show that the peak current of proton flux and the apparent voltages developed by this flux show the same saturation behavior as M_s, which is very different from that of both M_f and O. It is further shown that most of the proton-charge displacement is connected with the step M_s → BR. The optical and electrical data in these studies were collected simultaneously by a newly designed and built spectrometer which is described separately.

Kinetic analyses of bacteriorhodopsin (BR[1]) photocycle data have led to two distinctly different kinds of models (*1*). In one there is a single photocycle with reversible steps emanating from a homogeneous ground state, while the other has two or more independent photocycles originating from different forms of BR. While the single photocycle model is much more widely accepted, our laboratory has long been a subscriber to a model involving parallel photocycles. In a recent publication (*2*), the evidence for both kinds of models was presented in some detail, as well as the reasons for our favoring the parallel photocycle model.

The parallel photocycle for BR at pH near 7 and temperature near 20 °C consists of two separate cycles, one containing M_f and the other M_s.

$$BR \rightarrow K \rightarrow L_f \rightarrow M_f \rightarrow N \rightarrow O \rightarrow BR \quad \text{(M-fast)}$$

$$BR \rightarrow K \rightarrow L_s \rightarrow M_s \rightarrow BR \quad \text{(M-slow)}$$

where K, L, M, N, and O are the recognized intermediates of the BR photocycle and the subscripts "f" and "s" indicate the faster and slower time constants for intermediates displaying the same characteristic spectra. The maximum characteristic absorbance wavelengths for these individual spectra are listed in Table 1 of ref *2*.

In the M-fast cycle, M_f decays sequentially through N and O to BR, whereas in the M-slow cycle, M_s decays directly to BR. It has long been known that the saturation behaviors for M_f and M_s with respect to increasing energies of actinic light are quite different (*3*). Starting at very low levels of laser strength, M_f rises faster than M_s. Then, as laser strength is increased, M_f saturates sooner than M_s. Because of this behavior, the fraction of M_f relative to M_{tot} as a function of laser strength starts high and decreases while that of the fraction of M_s to M_{tot} starts low and rises. Based on the idea of two separate cycles, any intermediate contained within the M-fast cycle, when presented as a fraction relative to M_{tot}, should start high at the lowest levels of laser strength and then decrease with stronger actinic pulses whereas any intermediate in the M-slow cycle should show the opposite behavior. In this paper, we verify that expectation by showing that the fraction of O/M_{tot} behaves like the fraction M_f/M_{tot}.

Using the procedures of Kesthelyi and Dér and their collaborators (*4, 5*), one can measure the proton current which flows during a single turnover of BR. This is accomplished by orienting the purple membrane (PM) in an electric field in an optical cuvette and holding this orientation by forming an acyrlamide gel of the oriented population. The current is measured using two platinized electrodes and a suitable amplifier. Simultaneously, the optical changes are measured on the same sample. Both the time-resolved electrical and optical measurements can be fitted to exponentials. The membrane potential developed in each transition

[†] This research was supported by the Intramural Research Program of the NIH, National Heart, Lung, and Blood Institute.

[‡] Certain commercial equipment, instruments, or materials are identified in this paper to foster understanding. Such identification does not imply recommendation or endorsement by the National Institutes of Health or the National Institute of Standards and Technology, or that the materials and equipment are necessarily the best available for the purpose.

* Corresponding author. Phone: 301 572 5017. Fax: 301 402 1519. E-mail: rwh@helix.nih.gov.

[§] Laboratory of Cell Biology, National Heart, Lung, and Blood Institute, National Institutes of Health.

[||] Biospectroscopy Group, Biochemical Science Division, National Institute of Standards and Technology.

[1] Abbreviations: BR, ground state of bacteriorhodopsin; M_f, fast form of M-intermediate which decays to the O-intermediate with a time constant near 2 ms at pH near 7 and T near 20 °C; M_s, slow form of M-intermediate which decays to the BR with a time constant near 5 ms at pH near 7 and T near 20 °C; M_{tot}, sum of M_f and M_s; SVD-lsq, singular value decomposition based least-squares analysis; ADC, analog to digital voltage converter.

10.1021/bi701748n CCC: $40.75
Published on Web 04/19/2008

of the photocycle is proportional to the product of the amount of current and the distance through which it is moved. Using the fractions of both the peak currents and the proportional voltages formed as fractions relative to M_{tot}, we have determined that the saturation behaviors for electric current of protons and the voltages developed display the saturation behavior of the fraction of M_s/M_{tot} and are distinctly different from those of both M_f/M_{tot} and O/M_{tot}. By mathematical modeling we confirm that the M-slow cycle is the major contributor to electrogenic proton-pumping.

EXPERIMENTAL PROCEDURES

1. Preparation of Purple Membrane (PM). PM was isolated from the ET1001 strain of *Halobacterium salinarum* by the procedure of Oesterhelt and Stoeckenius (*6*) as modified by Mukhopadhyay et al. (*7*). For kinetic studies, 0.5 mg of BR in PM was suspended in 3 mL of 50 mM potassium phosphate buffer at pH 7.2 and 21 °C.

2. Optical Data Collection and Analysis. Time-resolved multichannel data were collected as previously described (*8, 9*). Light adaptation was obtained and maintained by constant illumination from the monitoring light source operated at 80 mW (Proton Technology International (PTI) 75 W xenon arc lamp model A1010, powered by a PTI LPS 220). There was no evidence of any significant amount of dark-adapted photocycle, such as the peak for BR being blue-shifted or the presence of an intermediate with a decay time constant near 30 ms. The fitted kinetic constants we obtained are in agreement with those published in the literature by other laboratories (*10–13*). Instead of the previously described spectrophotometric system (*14*), a new updated version of the instrument, as described separately, was used (*J. Biochem. Biophys. Methods*, doi: 10.1016/j.prot.2007.11.004). In this second-generation 96-channel spectrophotometer, certain improvements were obtained, namely, higher resolution (16 bits), higher maximum sampling rate (200 kHz), independent programmable gain and offset for each analog channel, logarithmic as well as linear scheduling of samples, and higher system reliability. Analysis of the data was performed using singular value decomposition-based least-squares (*15*) (SVD-lsq), based on multiexponential fittings of the time-course vectors in the SVD-derived V-matrix (*15, 16*). The OD amounts of individual components were obtained from the amplitudes of the SVD-reconstructed spectra at their characteristic maximum wavelengths. The data shown in this paper were collected from a series of ten experiments using two gels and five different levels of laser energy obtained by the use of 0, 0.2, 0.5, 1.0, and 1.5 neutral density filters to attenuate the beam. One hundred turnovers at a repetition rate of 0.2 Hz were averaged for the 0, 0.2, and 0.5 OD filters, 150 turnovers for the 1.0 OD filter and 300 turnovers for the 1.5 OD filter. One gel was oriented in a voltage field, and the other was identical except for nonorientation, as described below. A second series of ten experiments confirmed the findings reported here (not shown).

Estimated Uncertainties for Optical Data. At all levels of laser intensity, five time constants were clearly resolved within the limits of the 100 kHz time resolution of our spectrophotometer. These were close to 0.05 ms, 0.15 ms, 0.4 ms, 1.8 and 5 ms. As previously described (*8*), the first four of these are attributed to the transitions, $L_f \rightarrow M_f$, $L_s \rightarrow M_s$, $N \rightarrow O$, and $M_f \rightarrow N$, respectively, and the transition at ≈5 ms is shared by the returns of both O and M_s to the ground state. In the case of the electric signal, the distinction between these two transitions is based on whether the response of the signal to increasing laser intensity resembles that of optical signal for M_f or M_s, which are quite different. The faster time constant at ≈0.006 ms seen in the earlier study (*8*) using PM suspensions is not seen in acrylamide gel preparations. However, with the same PM in suspension, this faster transition is present. The most obvious explanation is that the gel preparations produce more light-scattering that interferes with the resolution of this constant which is present only in the first few time samples. Standard errors and dependency values for fitting the data and are shown in Table 2 (Results). The dependency values guard against over parametrization, where more than the minimum number of exponentials are provided (*16*). As pointed out in ref *16*, a dependency of 10 or higher begins to be worrisome, 100 or higher being a strong indication that too many parameters are being used to explain the data. The low dependency values for the fits shown in Table 2 (Results) indicate the absence of superfluous exponentials used for fitting the data.

The difference spectrum that corresponds to each exponential transition was obtained by SVD-lsq. To quantify the M-intermediates, a wavelength range of 390 to 475 nm was fitted to a fourth degree polynomial. The OD amount of change was obtained from the magnitude of the ΔA at 412 nm. The same procedure was used for the O-intermediate using a wavelength range of 521 to 679 nm and a characteristic peak wavelength of 640 nm, and for BR using a wavelength range of 503 to 590 nm and a characteristic peak wavelength of 568 nm. The differences between these absorbances and the OD values of the SVD curve are presented in Table 2 as (possible) errors in the measurements.

3. Measurement and Analysis of Photocycle-Induced Proton Currents. As shown by Keszthelyi and Ormos (*4*), PM in a water suspension can be oriented in a small DC electric field so that the coordinated proton flow induced by a single laser flash can be measured by two Pt electrodes. Furthermore, the time-resolved electric signals can be fitted by a sum of exponentials and their time constants corresponded to those obtained based on optical changes in the same suspension. This work was extended by Dér et al. (*5*), who showed that once orientation has been achieved, the preparation can be stabilized in an acrylamide gel so that the electric field can be removed and the gel could be impregnated with a buffer of choice. Our procedure for preparation of PM in an acrylamide gel is the following:

1 Place two platinized Pt electrodes on two inner opposite sides of 1 cm × 1 cm × 4 cm plastic cuvette having four clear sides.
2 Add in sequence with proper mixing, 1.6 mL of highly purified H_2O (>18.2 MΩ resistance), 0.1 mL of PM containing 0.5 to 0.6 mg BR, 0.6 mL 30% acrylamide and 0.8% bis-acrylamide, 0.02 TEMED.
3 Apply a constant DC voltage field of 10 V across the electrodes and then mix in 0.18 mL of a solution of 40 mg/mL ammonium persulfate.

The suspension gels within two minutes, during which time the current flowing between the two electrodes falls from ≈45 mA to ≈25 mA. After puncturing a small hole in the bottom of the cuvette with a wide gauge hypodermic needle,

the gel is removed from the cuvette and soaked overnight in 50 mM potassium phosphate buffer of pH 7.2.

For measurements, the washed gel is reinserted into the cuvette used for casting, with the orientation preserved. Two platinized Pt electrodes in the form of loops to fit the optical sides of the cuvette are inserted. The electric signals are amplified using a circuit comparable to those described by Keszthelyi and Ormos (*4*) and Dér et al. (*5*). Controls to monitor the electrode responses to the laser flashes used the above procedure without the DC-orienting electric field. The electric responses were extremely small, but nonetheless were subtracted from those obtained with the corresponding oriented gel. During an experiment, both the multichannel optical data and electrical data were simultaneously gathered from the same sample and stored. The electrical data were fitted to a sum-of-exponentials model.

According to Keszthelyi and Ormos (*4*), the "protein electric response signal" (PERS) represents the proton current which is converted to a voltage by passing it through an external resistance, *R*. The measured signal is therefore read as a voltage. This signal for each component as a function of time is represented by the expression

$$V_i(t) = (NRQd_i/D)k_i f_i(k_i,t) \quad (1)$$

where $V_i(t)$ is proportional to current of component i at time t and is measured as a voltage after passing through the resistor R; N = number of flash-excited BR photocycles = 14.34×10^{14}; R = value of input resistor in ohms = 230; Q = charge on a single proton in coulombs = 1.60×10^{-19}; d_i = displacement distance of proton from its neutralizing negative charge for component i; D = distance of separation of the measuring electrodes = 0.8 cm; k_i = kinetic constant for exponential decay of component i; $f_i(k_i,t) = \exp(-k_i t)$.

N was estimated from the amplitude at 568 nm of the difference spectrum that was obtained by least-squares SVD for the component with tau = 5.1 ms. This is the only time constant in the photocycle where the ground-state BR is regenerated from the fraction of BR that turns over after a laser pulse. This amplitude was 50 mOD. Using a molecular weight of 26784 Da, a molar extinction coefficient of 63000, and Avogadro's number, *N* was evaluated at 14.34×10^{14}. *Q*, in coulombs, is a universal constant that is equal to 1.60×10^{-19} (the Avogadro constant divided by 96494). $V_i(t)$ and k_i are computed by fitting the raw data to the sum-of-exponentials model. For any single state, *i*, eq 1, at $t = 0$, is simply

$$V_i(t) = (NR/D)Q d_i k_i \quad (1a)$$

or

$$V_i(t)\tau_i = PQd_i \quad (1b)$$

where

$$P = (NR/D)$$

Equation 1b shows that the local voltage formed by moving the charge through a distance d_i is proportional to the measured current, V_i, multiplied by its tau. The amplitude of V_i as well as the corresponding tau is obtained by curve-fitting the acquired data to a sum of exponentials. The time-resolved electrical data were acquired over the time range 0 to 189 ms with a time resolution of 10 μs. Before fitting, the trace was corrected for the small signals obtained for a parallel unoriented gel. The amplifier gain was calibrated with a square wave input at 1000 Hz and was determined to be 770 with the offset control at zero and 800 when a positive offset was used. The output voltage was then fed to one of the unused channels in the data acquisition module of the spectrometer described separately. This insures the simultaneity of the timing schedule for both the electric and optical data collected from the sample. The electrical data were digitized by a 16-bit, 10 V, analog to digital, bipolar converter (ADC). In order to avoid data that may have drifted below zero in the output of the amplifier, the offset was set to $\approx$+10 mV.

After multiexponential curve fitting, all of the quantities in eq 1, except d_i, are known. At $t = 0$, eq 1 can be rearranged to

$$d_i = (V_i(0)\ D)/(NRQk_i) \quad (1c)$$

Using the values for *N*, *R*, *Q*, and *D* given above, we have

$$d_i = \left(V_i(0) \times 0.8 \times 10^{-2}\right)/\left(14.34 \times 10^{14} \times 230 \times 1.6 \times 10^{-19} \times k_i\right)$$

$$d_i = 0.1516 V_i(0)/k_i \quad (1d)$$

$V_i(0)$, the current amplitude, after being converted to volts by passing through the 230 Ω resistor is acquired in counts after amplification and digitization. To convert the counts to input voltage, it is necessary to divide by 65536 (16-bits) and multiply by 10 (volts) and then finally to divide by the amplifier gain of 800.

$$V_i(0)\ (\text{volts}) = V_i(0)\ (\text{counts}) \times 1.9073 \times 10^{-7}$$

Equation 1d expressed with $V_i(0)$ in volts is

$$d_i = V_i(0)\ (\text{counts}) \times 2.8915 \times 10^{-8}/k_i \quad (1e)$$

For example, the component with tau of 5.13 ms (k_i = 195 s^{-1}) had an amplitude of 42 counts. Using eq 1e, d_i was evaluated as 6.23 nm. The d_i corresponding to the other taus can be evaluated in the same way.

RESULTS

1. Saturation Behaviors. A. Optical Data. Table 1 shows the magnitudes of OD changes for intermediates M_f, M_s, and their sum (M_{tot}), as well as for O and the total amount of BR that cycled at each level of laser energy. A graphic representation of these data is shown in Figure 1. The familiar relative saturation behaviors of M_f and M_s (*3*) are illustrated, namely, that M_f rises more rapidly with laser strength at very low laser energy and saturates sooner than M_s at higher energies. It is also shown that the saturation behavior of the O-intermediate (points shown as "*") closely resembles that of M_f in contrast to that of M_s. The absorbances for O were normalized to be comparable to those of M_f by multiplying by the empirically determined factor of 0.59. The difference in saturation characteristics for M_f and M_s is more strikingly illustrated when both are expressed as fractions relative to total M as shown in Figure 2. The fraction of M_f/M_{tot} starts high and decreases with laser strength while the fraction M_s/M_{tot} starts low and increases. The fraction of O/M_{tot} clearly resembles that of M_f/M_{tot} and is distinct from that of M_s/M_{tot}. This is to be expected since both M_f and O occur in

Table 1: Changes in Absorbance at Different Actinic Laser Energies

laser strength (mJ)	intermediate	ΔOD	error (OD)
18	M_f	1.2983e−2	3.0708e−4
	M_s	1.5270e−2	6.0081e−4
	O	2.3554e−2	2.5355e−4
	BR	4.9883e−2	1.2719e−4
11	M_f	1.1499e−2	3.3288e−4
	M_s	1.2581e−2	6.0028e−4
	O	2.0483e−2	2.2569e−4
	BR	4.2710e−2	1.0197e−4
6.1	M_f	9.7255e−3	1.7591e−4
	M_s	9.6308e−3	4.7353e−4
	O	1.6928e−2	1.9867e−4
	BR	3.3510e−2	8.4617e−5
2.2	M_f	5.7788e−3	1.4928e−4
	M_s	4.6439e−3	2.7209e−4
	O	9.5540e−3	8.3965e−5
	BR	1.7635e−2	4.3195e−5
0.74	M_f	2.8935e−3	4.1098e−5
	M_s	1.9102e−3	1.1875e−4
	O	4.6285e−3	5.0571e−5
	BR	7.7843e−3	2.2642e−5

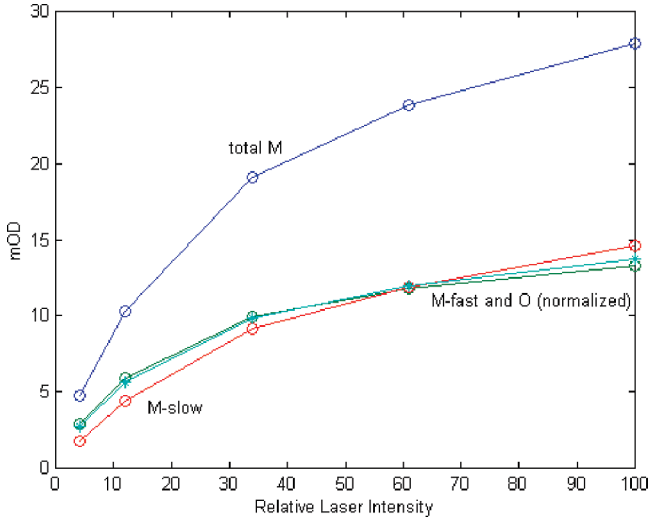

FIGURE 1: Saturation curves for M and O intermediates. Full laser strength was ≈18 mJ/2 cm^2.

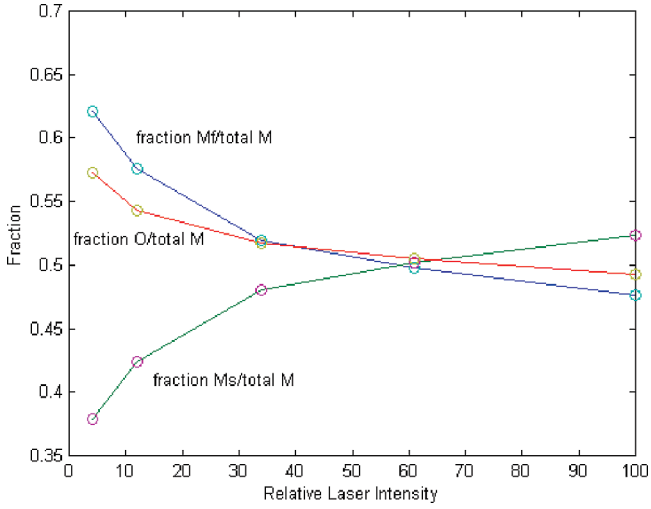

FIGURE 2: Saturation curves for fractions of M_f, M_s, and O relative to total M.

the same M-fast photocycle while that of M_s occurs without O in the M-slow photocycle. The expression of the same data as ratios in Figure 2, magnifies the small experimental difference shown in Figure 1. The demonstration in Figures 1 and 2 shows that the saturation behaviors for components of the M-fast and M-slow photocycles are sufficiently distinctive to serve as a basis for trying to associate the saturation behavior for electrogenic proton-pumping to either one, or relatively to both, of the two photocycles of BR.

Table 2: Fitting of Optical Kinetic Data

laser strength (mJ)	kinetic constant (ms^{-1})	error (ms^{-1})	dependency	tau (ms)
18	2.2045e1	1.0488e0	1.9468e0	4.5362e−2
	7.7797e0	3.4724e−1	2.0062e0	1.2854e−1
	2.7478e0	1.5369e−1	1.5345e0	3.6393e−1
	5.3831e−1	4.9255e−3	1.4427e0	1.8577e0
	1.8972e−1	4.9986e−4	1.1055e0	5.2710e0
11	1.9494e1	1.4907e0	2.2279e0	5.1298e−2
	6.4264e0	8.3320e−1	2.5255e0	1.5561e−1
	3.0743e0	4.4159e−1	1.8166e0	3.2527e−1
	5.2961e−1	8.3157e−3	1.4037e0	1.8882e0
	1.9350e−1	9.7207e−4	1.1479e0	5.1681e0
6.1	2.1425e1	1.8100e0	1.9252e0	4.6675e−2
	7.2673e0	6.8904e−1	2.0850e0	1.3760e−1
	2.6576e0	3.1979e−1	1.5866e0	3.7628e−1
	5.4301e−1	1.0000e−2	1.4809e0	1.8416e0
	1.9313e−1	1.0989e−3	1.1375e0	5.1779e0
2.2	1.9682e1	9.6641e−1	1.9176e0	5.0807e−2
	6.6718e0	5.0636e−1	2.1505e0	1.4988e−1
	2.6718e0	2.2759e−1	1.6827e0	3.7428e−1
	5.3344e−1	6.3059e−3	1.4800e0	1.8746e0
	1.9315e−1	7.8347e−4	1.1378e0	5.1773e0
0.74	1.6742e1	1.9375e0	2.2168e0	5.9731e−2
	6.8943e0	1.1698e0	2.1214e0	1.4505e−1
	1.7258e0	3.0533e−1	1.8740e0	5.7945e−1
	5.5179e−1	2.0417e−2	1.8381e0	1.8123e0
	1.9387e−1	1.8606e−3	1.1588e0	5.1580e0

At each level of actinic strength, we found that five kinetically distinct species were present (Table 2). These are essentially the same components as obtained previously by us (*2, 8*) and by Chizhov et al. (*13*) using optical data, and by Rodig et al. (*14*) and Morgan et al. (*15*) using FTIR data and by Müller et al. using both optical and FTIR data (*16*).

B. Electric Data. The raw data for proton currents generated by actinic pulses of different strengths are shown in the range of 0 to 1 ms in Figure 3 and from 0 to 8 ms in Figure 4.

From the data shown in Figures 3 and 4, one can obtain the magnitude of peak current as a function of actinic laser strength. As shown in Experimental Procedures (eq 1b), the product of the fitted time constant and maximum amplitude for each kinetic intermediate is proportional to the product of charge times distance, or the anticipated local voltage change. We refer to this product as the "integrated voltage". For the data shown in Figures 3 and 4, we were able to fit five kinetic components as shown in Table 3. Figure 5 shows the saturation behaviors for peak proton currents and relative integrated voltages developed for the fitted exponentials of the photocycle.

At each level of laser strength, three sets of fitted taus were obtained from the time-resolved kinetic data. Two were from the optical measurements, one for the oriented gel and one for the unoriented gel that served as a control for any electrode responses emanating from the laser flash instead of from the photocycle kinetics. The third set was obtained by fitting the time-resolved proton current data. For all fittings of proton current, the electrode response in the corresponding unoriented gel was subtracted. Table 4 shows the fitted taus

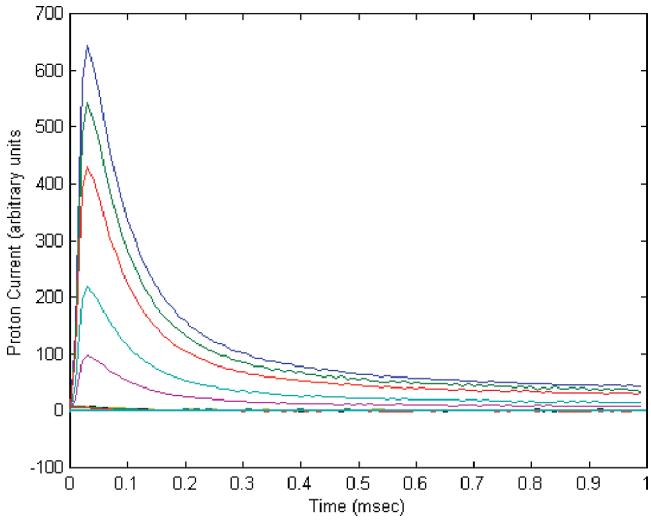

FIGURE 3: Time courses from 0 to 1 ms for electric signal at different energies of actinic laser pulse. The traces from top to bottom show the current generated by a laser pulse using 0, 0.2 ND, 0.5 ND, 1.0 ND, and 1.5 ND filters to block the actinic light. These data were collected using BR in gels oriented in an electric field. Corresponding traces with the same series of ND filters and unoriented BR in gels are all overlapped on or near the zero line.

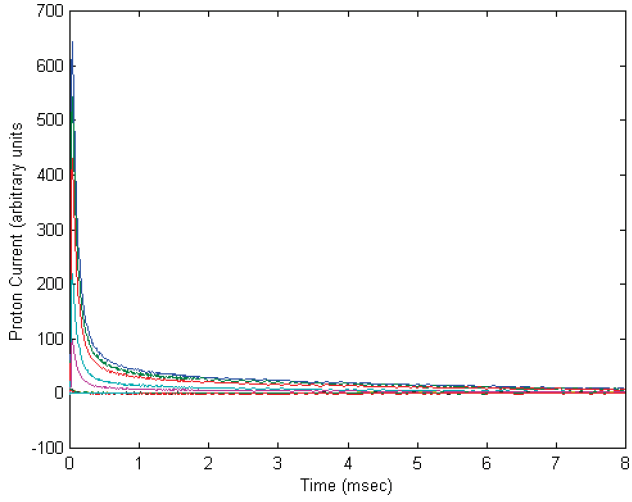

FIGURE 4: Time courses from 0 to 8 ms for electric signal at different energies of actinic laser pulse. Data shown in Figure 3 extended to 8 ms.

Table 3: Fitting of Electrical Kinetic Data

k (ms^{-1})	errors (ms^{-1})	dependencies	tau (ms)	amplitude	tau × amplitude
1.2497e2[a]	7.2466e−1	1.4956e0[b]	8.0019e−3	2.6386e3[c]	2.1114e1[d]
1.4614e1	2.4719e−1	3.8027e0	6.8429e−2	−8.1095e2	−5.5493e1
5.1782e0	7.9141e−1	5.6264e0	1.9312e−1	−1.1802e2	−2.2791e1
1.7916e0	2.3552e−1	4.0472e0	5.5817e−1	−4.4310e1	−2.4733e1
1.9487e−1	3.7056e−3	1.8674e0	5.1317e0	−4.1709e1	−2.1404e2

[a] e2 indicates ($\times 10^2$). [b] Dependency values below 10 combined with a low error indicate that the exponential is needed. [c] Amplitude for the exponential at time = 0. [d] Proportional to potential voltage generation as in eq 1b in Experimental Procedures.

obtained at the highest level of actinic strength for the electrical data from an oriented acrylamide gel and for optical data obtained from oriented, nonoriented gels and suspensions. The column labeled "Vtau" in the table is the fitted amplitude times the time constant, which is proportional to voltage resulting from charge separation as shown in eq 1b

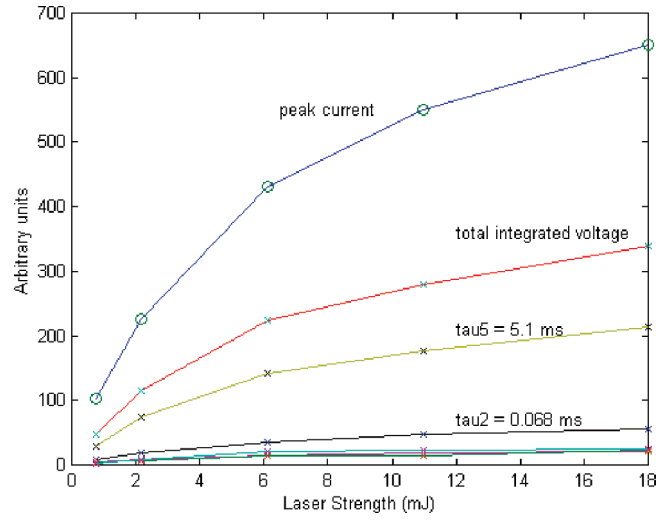

FIGURE 5: Saturation behaviors for peak currents (upper curve) and integrated (amplitude × tau) voltages for the total and all individual components. The three lowest curves are for taus 1, 3, and 4 shown in Table 4. The total integrated voltage is for the sum of all 5 taus shown in Table 4.

Table 4: Comparison of Fitted Taus

tau	electrical (oriented gel) ms	electrical (oriented gel) Vtau[a]	optical (oriented gel) ms	optical (unoriented gel) ms	optical (suspension) ms
1	8.0019e−3	21			7.7684e−3
2	6.8429e−2	55	4.5362e−2	4.3234e−2	5.8129e−2
3	1.9312e−1	23	1.2854e−1	1.2699e−1	1.6849e−1
4	5.5817e−1	25	3.6393e−1	3.8051e−1	4.7218e−1
5(optic)			1.8577e0	1.8442e0	2.1037e0
5(elec) 6(optic)	5.1317e0	214	5.2710e0	4.6818e0	4.7841e0

[a] Maximum value for current (amplitude) × (tau) using digitized data after amplification, which is proportional to voltage formed (Experimental Procedures; eq 1b).

(Experimental Procedures). The digitized values for the fitted amplitudes and taus were used after amplification as described in Experimental Procedures. Of the total of 338 for Vtau, the relative percent associated with each of the five electrical components in order was 6.2, 16.2, 6.8, 7.4, and 63.

Essentially the same taus were found at all levels of laser strength (not shown). The fastest tau at about 0.008 ms, which is attributed to the unresolved BR → K → L steps, is seen in the electric signal and in the optical data obtained with PM in suspension, but not with the optical signals obtained from the PM in gels. We suspect that additional light scattering in the gels interferes with obtaining an adequate fit to this fastest transition which is recorded in only the first 3 or 4 time samples. The electrical data show no component for M-fast decay at ≈2 ms, which is always seen in the optical data and is the decay time constant for the $M_f \rightarrow N$ transition (*2, 8*). Therefore, there is one less exponential required for fitting the electrical data than the optical data. No time constant longer than the ≈5 ms component was seen in the optical data. In the electrical data, there was a long slow, small, and inconsistent electrode drift that we fitted in order to remove any influence on the ≈5 ms component.

Figure 6 shows the saturation behavior for the sum of the apparent voltages for the fitted taus numbered from 1 to 5

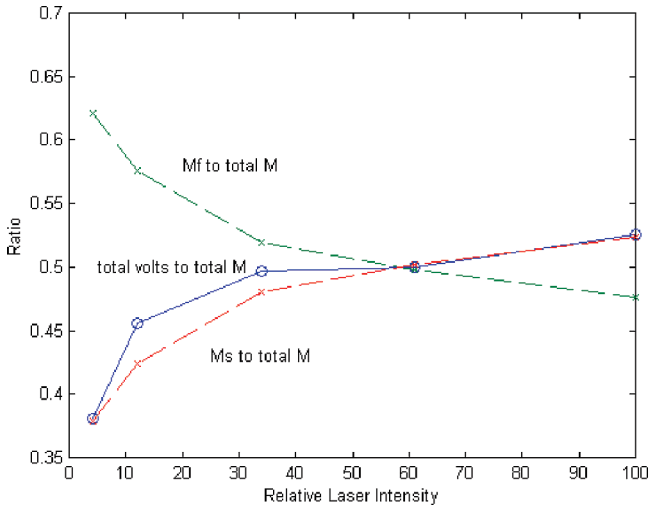

FIGURE 6: Saturation behaviors of fractions of M_f, M_s, and total integrated volts (see Figure 5) relative to total M.

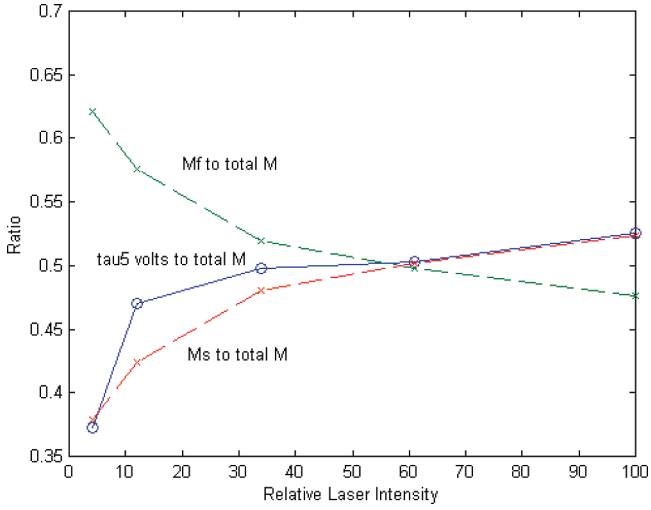

FIGURE 7: Saturation behaviors of fractions of M_f, M_s, and tau5 integrated volts (see Figure 5) relative to total M.

in Table 4, expressed as a fraction relative to total M. For comparison purposes, the fractions of M_f/M_{tot} and M_s/M_{tot} from Figure 2 are also shown. The arbitrary units for the fraction of total voltage relative to total M were scaled to be comparable to those for the fractions M_f/M_{tot} and M_s/M_{tot}. It is seen that the saturation behavior for the fraction volts/M_{tot} more closely resembles the fraction of M_s/M_{tot} than that of M_f/M_{tot}. However, at the lowest levels of laser energy, some additional voltage, above that expected from M-slow cycle alone, is evident.

As illustrated in Figure 5 and Table 4, the most quantitatively significant voltage formation accompanies the transition with tau near 5 ms, which in the M-slow cycle is the $M_s \rightarrow$ BR step and in the M-fast cycle is the O $\rightarrow$ BR transition. To assess the possible role of this transition in the voltage produced at low laser strengths, the fraction of tau5 volts relative to M_{tot} was scaled to the units for the fractions of M_f and M_s relative to M_{tot}. Figure 7 shows that some of the additional proton-pumping activity at lower laser strengths (compared to that expected from the M-slow cycle alone) is contributed by this transition. The next most significant voltage formation accompanies the transition with tau near 0.068 ms and is attributed to the conversion of $L_f \rightarrow M_f$ in the M-fast cycle (*2, 8*). Just as was done for the

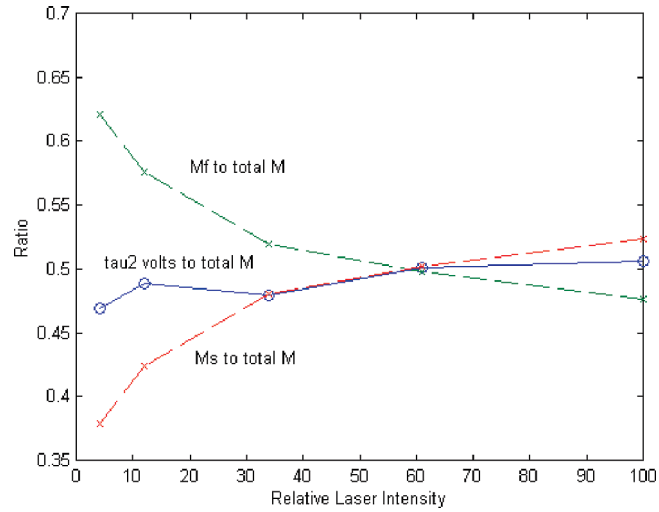

FIGURE 8: Saturation behaviors of fractions of M_f, M_s, and tau2 integrated volts (see Figure 5) relative to total M.

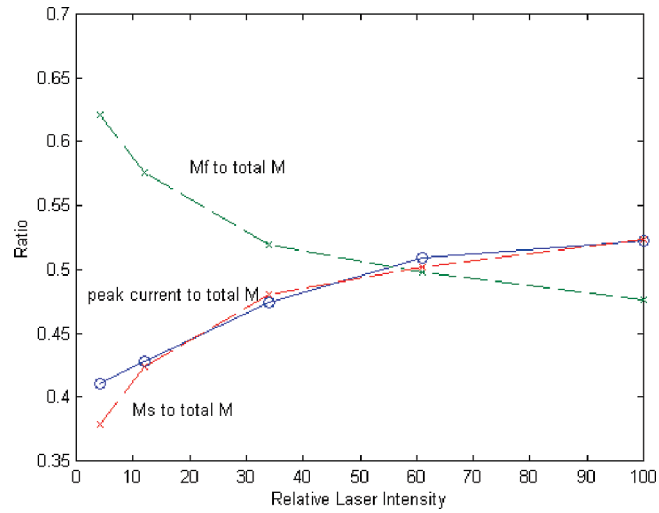

FIGURE 9: Saturation behaviors of fractions of M_f, M_s, and peak current (see Figure 5) relative to total M.

fraction of tau5 volts relative to M_{tot}, the fraction for tau2 volts was scaled to match the units for the M_f and M_s fractions. Figure 8 shows that some of the additional voltage at low laser strength was also contributed by this 0.068 ms transition. Figure 9 shows that the saturation behavior for the scaled amount of peak current relative to M_{tot} very closely follows the saturation behavior for the fraction M_s/M_{tot}.

Figures 6−8 show that, at low laser intensity, the M-fast cycle does contribute to the cumulative electrogenic changes. To gain more information on the relative amounts of pumping by the M-fast and M-slow cycles, we modeled the saturation curve behavior shown in Figure 1 for M_s and M_f with "pumping coefficients" to approximate the saturation behavior for the total integrated voltage as shown in Figure 5. That is,

$$p1 * M_s + p2 * M_f = \text{total integrated voltage}$$

where p1 and p2 are relative pumping efficiencies of the two cycles. The fitted coefficients were

	parameters	errors	dependencies
M_s	1.6287e+001	1.9515e+000	9.1223e+000
M_f	4.9162e-001	1.6358e+000	9.1223e+000

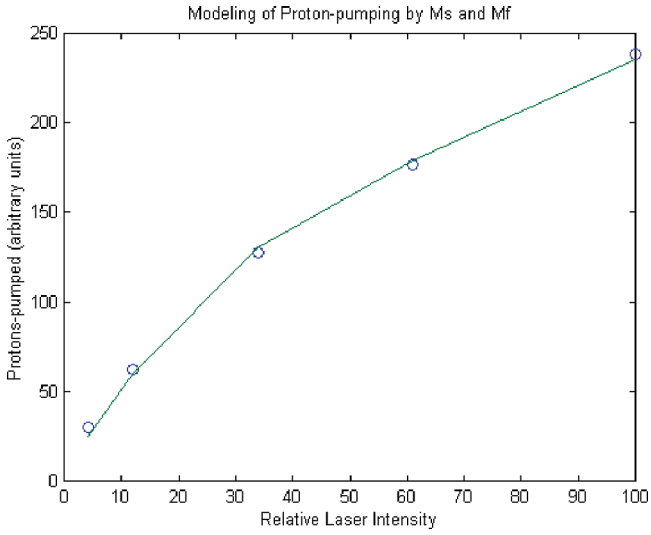

FIGURE 10: Total integrated voltage modeled from the contributions of M_f and M_s. The curve shows the saturation behavior for the total integrated voltage (see Figure 5). The points are from the combination of saturation curves for M_f and M_s as shown in Figure 1, and the line is based on the coefficients obtained by least-squares fitting as shown in the text.

Table 5: Calculation of Charge Separation (d_i) for Each Fitted Tau

	tau (ms)	$V_i(0)$ (counts)	k_i (s^{-1})	d_i (nm)	%
1	0.008	2639	1.25×10^5	0.61	6.2
2	0.068	811	1.46×10^4	1.61	16.5
3	0.193	118	5178	0.66	6.8
4	0.558	44	1792	0.71	7.3
5	5.13	42	195	6.23	64

The points in Figure 10 show the raw data for total protons pumped, and the line is the modeled total using the fitted coefficients. It is obvious that the M-slow cycle is a major contributor to the overall electrogenic pumping capability of the system.

2. Further Analysis of Proton Current Data. As discussed in Experimental Procedures, using the equation of Keszthelyi and Ormos (*4*), one can compute the amount of charge separation d_i for each stage of proton transfer during the photocycle(s). The acquired data at 10 μs resolution were fitted by five exponentials. The corresponding d_i values obtained by using eq 1e in Experimental Procedures are shown in Table 5. The sum of d_i is 9.8 nm, which is very close to the 10.5 nm found by Keszthelyi and Ormos (*4*) and is about twice the expected 5 nm for the nominal thickness of a lipid bilayer. Keszthelyi and Ormos used gels hydrated with distilled water and fitted the data to four exponentials with taus of 0.004 ms, 0.081 ms, 2.5 ms, and $\approx$8 ms. Our gels were equilibrated with 50 mM potassium phosphate at pH 7.2, and the data were fitted to five exponentials (Table 5). It is not unexpected to find the same apparent membrane thickness from both sets of data. Keszthelyi and Ormos pointed out that their finding of 10.5 nm was about twice the expected thickness for a lipid bilayer. The usual cellular membrane as described by Singer and Nicolson (*17*) in their fluid mosaic model contains stretches of lipid bilayer with proteins either embedded in one side or the other or penetrating the entire bilayer with protrusions on both sides. The bilayer portion of the membrane is $\approx$5 nm in thickness. Purple membrane patches, however, are predominantly protein which comprises 75% by weight of the PM. There are 30 lipid molecules per trimer that are associated with the protein in specific functional linkages. Most of the surface is covered with tightly packed trimers in hexagonal array. There is no continuous extent of bilayer as seen in average cell membranes. Müller et al. (*18*), using atomic force spectroscopy, showed that the trimer units extended $\approx$0.6 nm above the bilayer on the extracellular surface and about 1 nm on the cytoplasmic surface. Therefore the overall distance for proton movement is probably closer to 6.6 nm than 5 nm. Still, the sum of d_i from Table 5 is almost double that of 6.6 nm. In their 1980 paper, Keszthelyi and Ormos (*4*) suggested that the finding of a sum of d_i about twice that expected could mean that two protons instead of one were translocated in every photocycle. Now, 26 years later, it seems less likely that this is the cause of the double length obtained by summing all of the d_i distances. The summation listed in Table 5, as well as the calculations of Keszthelyi and Ormos (*4*), are based on the idea that there is a single homogeneous photocycle where all of the fitted exponentials represent sequential steps. The alternative view, favored by our laboratory, is that at pH 7 and near 20 °C, there are two separate cycles, one containing M-fast and the other M-slow. According to the results presented in this paper, the M-slow cycle is responsible for most of the proton-pumping. With the 10 μs resolution employed here, there are three isolated steps in this cycle, namely, BR $\rightarrow$ L $\rightarrow$ M $\rightarrow$ BR. The successive taus for these three steps are listed in rows 1, 3, and 5 of Table 5. The sum of the d_i 's for these steps is 7.5 nm, which is quite close to the 6.6 nm expected. As a matter of fact, the small difference is within a reasonable range of uncertainty. The distance between the two electrodes, D, is nominally set at 0.8 cm for the evaluation of eq 1e. But the Pt electrodes are inserted through the gel against the cuvette inner surfaces. If the effective distance between the two electrodes were 0.7 cm, the computed sum of d_i distances would be 6.6 nm. The dielectric constant for proteins is in the range of 1 to 4, which is quite similar to the dielectric constant for lipid bilayers, which is about 2.2 (*19, 20*). Therefore charge separation across the axis of the BR perpendicular to the membrane should lead to the same amount of voltage formation as that across the bilayer. The near agreement of the expected sum of d_i distances and the path length across the membrane-traversing bR presented here does not establish that the view presented here is correct, but it is worthy of further consideration.

DISCUSSION

The most striking difference in the two cycles of the parallel model is in the decay route from the M-intermediate to the ground state.

$$\text{M-fast cycle:} \quad R \rightarrow K \rightarrow L_f \rightarrow M_f \rightarrow N \rightarrow O \rightarrow BR$$

$$\text{M-slow cycle:} \quad BR \rightarrow K \rightarrow L_s \rightarrow M_s \rightarrow BR$$

The tau for the decay of M_f to N in the M-fast cycle is close to 2 ms (*2, 8*). In Table 4 it is seen that the apparent voltage formation for this step was 0. This finding confirms an earlier study by Müller et al. (*16*), who studied kinetics of PM using optical, FTIR, and photcurrent measurements. Their taus, by all procedures, were very close to those we report. Their 2.5 ms component, although prominent in both the optical and FTIR data, did not show any associated proton

current. The tau for the decay of N to O in suspensions of BR is usually close to 0.5 ms (*2, 8*). The relative amount of total apparent voltage for this transition was about 7% (Table 4). A tau near 5 ms is shared by both cycles for the reformation of the ground state (*2, 8*). As shown in Table 4, the transition with a tau of 5.1 ms accounted for about 63% of the total apparent voltage formation. One of the main aims of the current research was to see if the ambiguity in this common tau, in regard to proton-pumping ability, could be resolved. Based on the strikingly different saturation behaviors for the two cycles, it was possible to determine that a major fraction of the proton current and apparent voltage formation arises during the M-slow cycle (Figure 10). Therefore, it is concluded that the amount of voltage formation in the decay of O to the ground state is very much smaller than that which accompanies the decay of M_s to the ground state. However, about 24% of the total integrated voltage was associated with two transitions assigned to the M-fast cycle, notably the $L_f \rightarrow M_f$ step with tau near 0.068 ms and $N \rightarrow O$ with tau near 0.558 ms. One (speculative) proposal to account for this observation is that although the actual impetus for proton movement stems from the transitions of states in the M-slow cycle, local proton currents may be influenced by temporally changing global characteristics of the membrane such as resistance and capacitance. Exponential changes of protein conformation associated with certain steps in the M-fast cycle could then be translated into measurable changes in proton current which reflect these events.

It is also of interest to note in Table 4 that the time constants for transitions 2 ($BR \rightarrow L_f$), 3 ($BR \rightarrow L_s$), and 4 ($N \rightarrow O$) are somewhat delayed in the electrical measurements compared to the optical data for the oriented gel. We see two possible explanations for this. It may be associated with some time constant in the electronic measurement system or perhaps there is a slight lag between the change in environment responsible for optical shift and the actual physical movement of the proton in the gel system, which may be retarded by friction and localized membrane potential ($\Delta\Psi$) as described below.

A major finding, reported here, that the M-slow photocycle is primarily responsible for electrogenic proton-pumping is the opposite of the view we formerly proposed, namely, that the M-fast cycle is more likely to be predominant in proton-pumping (*9*). This earlier conclusion was based primarily on two observations: First, protonophore uncouplers increased the ratio of M_f/M_s in whole cells and in isolated closed systems where the electrochemical potential for protons ($\Delta\tilde{\mu}H^+$) was allowed to build. Because only tightly coupled systems are inhibited by $\Delta\tilde{\mu}H^+$ and subsequently speeded by uncouplers (*21*), it appeared that the M-fast cycle was tightly coupled to proton-pumping. Second, the ratio of M_f/M_s rises as the strength of the actinic laser pulse is decreased. At low levels of activating light, the M-fast cycle is predominant, and at high light levels, the M-slow cycle predominates. A light-level regulation of this kind could ensure the highest level of energy conversion at very low light levels and offer protection against excessive amounts of voltage on the membranes at the highest light levels. The results reported here refute our earlier proposal.

The finding that the M-fast cycle was deficient in its ability to electrogenically pump protons does not necessarily mean that it is unable to pump protons to form a pH gradient. It is important to note that the energy transduced and stored by a proton pump consists of two forms: one, the electrical component $\Delta\Psi$, and the other, the chemical component ΔpH. The same amount of energy in an electrochemical gradient for protons ($\Delta\tilde{\mu}H^+$) can be present with markedly different relative amounts of these two components. This is illustrated by the fact that with BR-liposomes, most of the developed $\Delta\tilde{\mu}H^+$ is in the form of a ΔpH (*22–24*), whereas in whole cells of *H. salinarum*, most is in the form of $\Delta\Psi$ (*24*). The relative amounts of the two components could be dramatically changed by addition of specific ionophores and exchangers for K^+ and H^+ or agents that relieve or enhance the $\Delta\tilde{\mu}H^+$ formed from respiration or the diffusion potential for K^+ (*16–20*). It has been amply demonstrated that a high $\Delta\Psi$ impedes proton-pumping that leads to a ΔpH (*16–21*) and that agents that deplete $\Delta\Psi$ lead to enhanced proton pumping across the membrane (*21–25*). The parallel cycles model is based on a topographical separation of M-fast cycles and M-slow cycles in the membrane, due to unique lipid–protein associations and interactions. This view is supported by the domain organization view of biological membranes as discussed in ref *2* and the demonstration of the dependence of the relative turnovers of M_f and M_s on the overall hydrophobicity of the membrane as well as interactions of specific purple membrane lipids with individual amino acid residues in bR, also discussed in ref *2*. In such a view of the membrane, the M-fast cycles could have localized areas of low $\Delta\Psi$, which would be favorable for nonelectrogenic proton-pumping leading to a ΔpH. One indication that this may be the case is that in an oriented PM-gel configuration, similar to the one used here, the amount of proton-pumping vs increasing fraction cycling (i.e., increased laser intensity) decreased (*26*). If only the M-slow cycle could pump protons, the opposite result would be expected. The reason for the decrease in medium acidification was attributed to the above-described phenomenon where rising $\Delta\Psi$ decreases the efficiency of proton movements that contribute to ΔpH (*26*).

Another important consideration is the significance of the factors just discussed on experimentally determined proton-pumping ratios based on measuring acidification of the external medium in relation to the rate of turnover of a particular chemical entity, such as an M or K intermediate in the BR photocycle or in the uptake of O_2 in respiratory systems. These factors become much more important when working with systems where $\Delta\Psi$ can build such as in cells, liposomes, and oriented membranes held in a gel. In these cases, the very earliest rates must be measured because the ratio for protons pumped decreases continuously as $\Delta\tilde{\mu}H^+$ rises (*27*). In the case of the BR photocycle, there is an additional complication in that there is a delay in the kinetics of proton release from the external surface relative to the turnover of any particular intermediate in the photocycle (*28, 29*). Furthermore, if there is a difference in the acidification of the external medium between protons pumped by the M-fast and M-slow cycles, then only an average ratio can be found.

The view of parallel cycles with different responses to actinic light and efficiencies for electrogenic and nonelectrogenic proton-pumping will have a bearing on the determination of quantum efficiencies, not only of BR turnover, but also of proton-pumping. Instead of a single quantum efficiency for turnover, there would be two. Instead of a

single efficiency for proton-pumping, there may be four: one each for electrogenic and nonelectrogenic pumping in the two cycles. Furthermore, since the ratios of both kinds of pumping are condition-dependent, the efficiencies may also be.

In addition to finding that the M-slow cycle appears to be predominant for electrogenic proton-pumping, the data indicate that the maximum amount of $\Delta\Psi$ development accompanies the transition at ≈5 ms where M_s decays to the ground state. This conclusion was based on the relative magnitudes of voltage formation expressed as the product of charge times distance of charge-separation for each transition. According to Song et al. (*30*), there is a major change in orientation of the Schiff base that occurs in the step O → BR that is coincident in time with the recovery of BR in the M-slow cycle. If this is reflective of a major change in protein conformation, it is possible that the electrical properties of the membrane may be changed to enhance both charge movement and voltage formation. At the moment, however, this is only an interesting possibility that requires experimental verification.

The main finding in this work is that the saturation behavior for electrogenic proton-pumping associated with the decay reactions linking M_f to BR is different from that which accompanies the decay of M_s to BR. This is in addition to the known differences in the saturation behaviors for the relative amounts of M_f and M_s which turn over during the photocycle and to the differences in their decay routes. All of these observations can be explained by separate photocycles containing each of the M-intermediates. We know of no way to explain these observations if there is only a single ground state for BR. No photocooperative scheme has yet been presented that can accommodate the above observations in a photocycle based on a single homogeneous ground state. In a separate paper (Hendler et al., ref *31*), we have examined the most predominant, published photocooperative models and found them inconsistent with experimental data obtained over a wide range of actinic light pulses. We also examined a newer form of homogeneous photocooperative model based on a branched photocycle where M_f and M_s are contained in separate pathways and multiple photon hits to a single target can alter the branching ratio. This model was far superior to any previously conceived homogeneous, photocooperative model, in its ability to produce results that were very close to those obtained experimentally. However, its homogeneous ground state predicts a monoexponential relationship between Mtot formation and laser intensity, whereas the experimental relationship requires two exponentials for fitting. It was also found that the formation of each M_f and M_s also requires two exponentials for fitting. This suggests an alternative view of the heterogeneous model in which the separate sequences containing M_f and M_s are present in branches. This idea is more fully explored in Hendler et al. (*31*).

ACKNOWLEDGMENT

We thank Lel Drachev for his generous help and guidance in the electrical measurements of proton current and Gary W. Kramer for his suggestions and continued support of the project.

REFERENCES

1. Zimanyi, L., Saltiel, J., Brown, L. S., and Lanyi, J. K. (2006) A Priori Resolution of the Intermediate Spectra in the Bacteriorhodopsin Photocycle: The Time Evolution of the L Spectrum Revealed. *J. Phys. Chem. A 110*, 2318–2321.
2. Hendler, R. W. (2005) An Apparent General Solution for the Kinetic Models of the Bacteriorhodopsin Photocycles. *J. Phys. Chem. B 109*, 16515–16528.
3. Shrager, R I., Hendler, R. W., and Bose, S. (1995) The ability of actinic light to modify the bacteriorhodopsin photocycle: Heterogeneity and/or photocooperativity. *Eur. J. Biochem. 229*, 589–595.
4. Keszthelyi, L, and Ormos, P. (1980) Electric Signals Associated with the Photocycle of Bacteriorhodopsin. *FEBS Lett. 109*, 189–193.
5. Dér, A., Hargittai, P., and Simon, J. (1985) Time-resolved photoelectric and absorption signals from oriented purple membranes immobilized in gel. *J. Biochem. Biophys. Methods 10*, 295–300.
6. Oesterhelt, D., and Stoeckenius, W. (1974) Isolation of the Cell Membrane of *Halobacterium holobium* and its Fractionation into Red and Purple Membrane. *Methods Enzymol. 31*, 667–679.
7. Mukhopadhyay, A. K., Dracheva, S., Bose, S., and Hendler, R. W. (1996) Control of the Integral Membrane Proton Pump, Bacteriorhodopsin, by Purple Membrane Lipids of *Halobacterium halobium*. *Biochemistry 35*, 9245–9252.
8. Hendler, R. W., Shrager, R. I., and Bose, S. (2001) Theory and Procedures for Finding a Correct Kinetic Model for the Bacteriorhodopsin Photocycle. *J. Phys. Chem. B 105*, 3319–3328.
9. Hendler, R. W., and Bose, S. (2003) Interconversions among four M-intermediates in the bacteriorhodopsin photocycle. *Eur. J. Biochem. 270*, 3518–3524.
10. Chizhov, I., Chernavskii, D. S., Engelhard, M., Mueller, K. H., Zubov, B. V., and Hess, B. (1996) Spectrally silent transitions in the bacteriorhodopsin photocycle. *Biophys. J. 71*, 2329–2345.
11. Rodig, C., Chizhov, I., Weidlich, O., and Siebert, F. (1999) Time-resolved Step-Scan Fourier Transform Infrared Spectroscopy Reveals Differences between Early and Late M Intermediates of Bacteriorhodopsin. *Biophys. J. 76*, 2687–2701.
12. Morgan, J. E., Vakkasoglu, A. S., Gennis, R. B., and Maeda, A. (2007) Water Structural Changes in the L and M Photocycle Intermediates of Bacteriorhodopsin as Revealed by Time-Resolved Step-Scan Fourier Transform Infrared (FTIR) Spectroscopy. *Biochemistry 46*, 2787–2796.
13. Müller, K. H., Butt, H. J., Fendler, K., Hess, B., Siebert, F., and Engelhard, M. (1991) The Reaction Cycle of Bacteriorhodopsin—An Analysis using visible absorption, Photocurrent and Infrared Techniques. *Eur. Biophys. J. 19*, 241–251.
14. Cole, J. W., Hendler, R. W., Smith, P. D., Fredrickson, H. A., Pohida, T, J., and Friauf, W. S. (1997) A high speed optical multichannel analyzer. *J. Biochem. Biophys. Methods 35*, 161–174.
15. Hendler, R. W., and Shrager, R. I. (1994) Deconvolutions based on singular value decomposition and the pseudoinverse: a guide for beginners. *J. Biochem. Biophys. Methods 28*, 1–33.
16. Shrager, R. I., and Hendler, R. W. (1998) Some pitfalls in curve-fitting and how to avoid them: A case in point. *J. Biochem. Biophys. Methods 36*, 157–173.
17. Singer, S. J., and Nicolson, G. L. (1972) Fluid Mosaic Model of Structure of Cell-Membranes. *Science 175*, 720–731.
18. Müller, D. J., Heymann, J. B., Oesterhelt, F., Möller, C., Gaub, H., Büldt, G., and Engel, A. (2000) Atomic force microscopy of native purple membrane. *Biochim. Biophys. Acta 1460*, 27–38.
19. Requina, J., and Haydon, D. A. (1975) Vanderwaals Forces in Oil-Water Systems from Study of Thin Lipid Films. 2. Dependence of Vanderwaals Free-Energy of Thinning on Film Composition and Structure. *Proc. R. Soc. London, Ser. A: Math. Phys. 347*, 161–177.
20. White, S. H. (1978) Formation of Solvent-Free Black Lipid Bilayer Membranes from Glyceryl Monooleate Dispersed in Squalenen. *Biophys. J. 23*, 337–347.
21. Westerhoff, H. V., and Dancshazy, Zs. (1984) *Trends Biochem. Sci. 9*, 112–117.
22. Hendler, R. W., Mukhopadhyay, A. K., Smith, P. D., and Cassio, H. E. (1996) A monitoring system for energy transduction by bacteriorhodopsin liposomes. *J. Biochem. Biophys. Methods 33*, 89–104.

23. Hellingwerf, K. J., Arents, J. C., Scholte, B. J., and Westerhoff, H. V. (1990) Bacteriorhodopsin in liposomes. II. Experimental evidence in support of a theoretical model. *Biochim. Biophys. Acta 547*, 561–582.
24. Rigaud, J. L., Bluzat, A., and Buschlen, S. (1983) Incorporation of bacteriorhodopsin into large unilamellar liposomes by reverse phase evaporation. *Biochem. Biophys. Res. Commun. 111*, 373–382.
25. Joshi, M. K., Bose, S., and Hendler, R. W. (1999) Regulation of the bacteriorhodopsin photocycle and proton-pumping in whole cells of *Halobacterium salinarium*. *Biochemistry 24*, 8786–8793.
26. Tóth-Boconádi, R., Taneva, S. G., and Kesthelyi, L. (2005) Actinic Light-Energy Dependence of Proton Release from Bacteriorhodopsin. *Biophys. J. 89*, 2605–2609.
27. Hendler, R. W., and Shrager, R. I. (1987) Problems in the experimental determination of substrate-specific H^+/O ratios during respiration. *J. Bioenerg. Biomem. 19*, 551–569.
28. Heberle, J., Riesle, G., Thiedemann, G., Oesterhelt, D., and Dencher, N. A. (1994) Proton Migration Along the Membrane-Surface and Retarded Surface to Bulk Transfer. *Nature 370*, 379–382.
29. Alexiev, U., Mollaghababa, R., Scherrer, P., Khorana, H. G., and Heyn, M. (1995) Rapid Long-Range Prototn Diffusion Along the Surface of the Purple Membrane and delayed Proton-Transfer into the Bulk. *Proc. Natl. Acad. Sci. U.S.A. 92*, 372–376.
30. Song, Q., Harms, G. S., Wan, C., and Johnson, C. K. (1994) Reorientations in the Bacteriorhodopsin Photocycle. *Biochemistry 33*, 14026–14033.
31. Hendler, R. W., Shrager, P. I., and Meuse, C. W. (2008) The Ability of Actinic Light To Modify the Bacteriorhodopsin Photocycle Revisited: Heterogeneity vs Photocooperativity. *Biochemistry 47*, 5406–5416.

BI701748N